



1 Bimodal or quadrimodal? Statistical tests for the shape of fault patterns

2 David Healy^{1*} & Peter Jupp²

3 ¹School of Geosciences, King's College, University of Aberdeen, Aberdeen AB24 3UE Scotland

4 ²School of Mathematics & Statistics, University of St Andrews, St Andrews KY16 9SS Scotland

5 *Corresponding author e-mail: d.healy@abdn.ac.uk

6

7 Abstract

8 Natural fault patterns, formed in response to a single tectonic event, often display significant
9 variation in their orientation distribution. The cause of this variation is the subject of some
10 debate: it could be 'noise' on underlying conjugate (or bimodal) fault patterns or it could be
11 intrinsic 'signal' from an underlying polymodal (e.g. quadrimodal) pattern. In this
12 contribution, we present new statistical tests to assess the probability of a fault pattern
13 having two (bimodal, or conjugate) or four (quadrimodal) underlying modes. We use the
14 eigenvalues of the 2nd and 4th rank orientation tensors, derived from the direction cosines of
15 the poles to the fault planes, as the basis for our tests. Using a combination of the existing
16 fabric eigenvalue (or modified Flinn) plot and our new tests, we can discriminate reliably
17 between bimodal (conjugate) and quadrimodal fault patterns. We validate our tests using
18 synthetic fault orientation datasets constructed from multimodal Watson distributions, and
19 then assess six natural fault datasets from outcrops and earthquake focal plane solutions. We
20 show that five out of six of these natural datasets are probably quadrimodal. The tests have
21 been implemented in the R language and a link is given to the authors' source code.

22

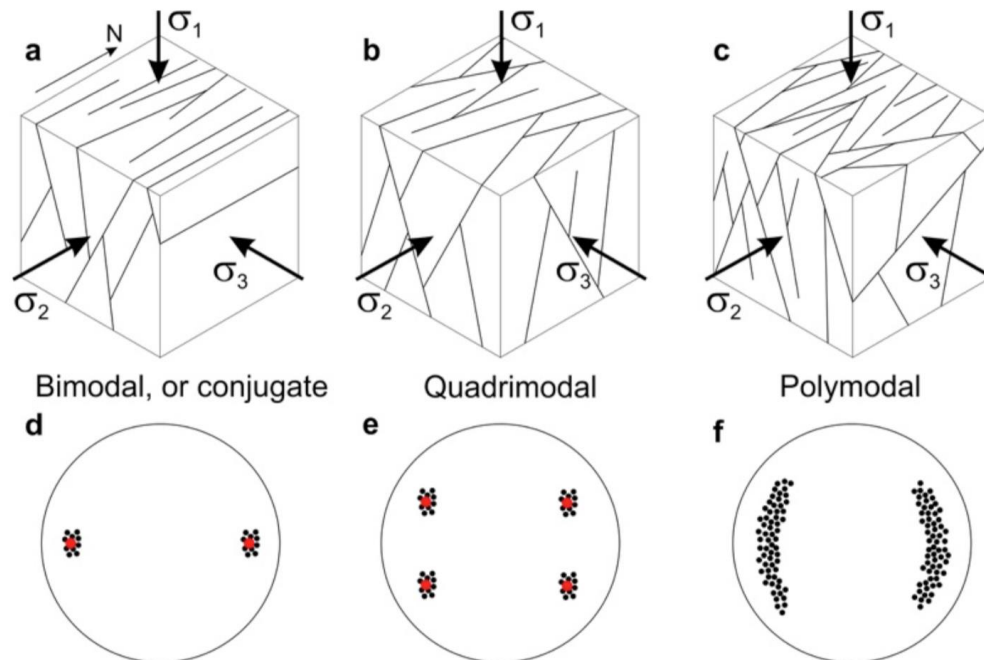
23 1. Introduction

24 1.1 Background

25 Faults are common structures in the Earth's crust, and they rarely occur in isolation. Patterns
26 of faults, and other fractures such as joints and veins, control the bulk transport and
27 mechanical properties of the crust. For example, arrays of low permeability (or 'sealing')
28 faults in a rock matrix of higher permeability can produce anisotropy of permeability and
29 preferred directions of fluid flow. Arrays of weak faults can similarly produce anisotropy – i.e.
30 directional variations – of bulk strength. It is important to understand fault patterns, and
31 quantifying the geometrical attributes of any pattern is an important first step. Faults, taken
32 as a class of brittle shear fractures, are often assumed to form in conjugate arrays, with fault
33 planes more or less evenly distributed about the largest principal compressive stress, σ_1 , and
34 making an acute angle with it. This model, an amalgam of theory and empirical observation,
35 predicts that conjugate fault planes intersect along the line of σ_2 (the intermediate principal
36 stress) and the fault pattern overall displays bimodal symmetry (Figure 1a). A fundamental
37 limitation of this model is that these fault patterns can only ever produce a plane strain
38 (intermediate principal strain $\epsilon_2 = 0$), with no extension or shortening in the direction of σ_2 .



39 This kinematic limitation is inconsistent with field and laboratory observations that
40 document the existence of polymodal or quadrimodal fault patterns, and which produce
41 triaxial strains in response to triaxial stresses (e.g. Aydin & Reches, 1982; Reches, 1978;
42 Blenkinsop, 2008; Healy et al., 2015; McCormack & McClay, 2018). Polymodal and
43 quadrimodal fault patterns possess orthorhombic symmetry (Figure 1b & 1c).



44

45 **Figure 1.** Schematic diagrams to compare conjugate fault patterns displaying bimodal
46 symmetry with quadrimodal and polymodal fault patterns displaying orthorhombic
47 symmetry. **a-c)** Block diagrams showing patterns of normal faults and their relationship to
48 the principal stresses. **d-f)** Stereographic projections (equal area, lower hemisphere) showing
49 poles to fault planes for the models shown in a-c. Natural examples of all three patterns have
50 been found in naturally deformed rocks.

51 Fault patterns are most often visualised through maps of their traces and equal-angle
52 (stereographic) or equal-area projections of poles to fault planes or great circles. Azimuthal
53 projection methods (hereafter 'stereograms') provide a measure of the orientation
54 distribution, including the attitude and the shape of the overall pattern. However, these plots
55 can be unsatisfactory when they contain many data points, or the data are quite widely
56 dispersed. Woodcock (1977) developed the idea of the fabric shape, based on the fabric or
57 orientation tensor of Scheidegger (1965). The eigenvalues of this 2nd rank tensor can be used
58 in a modified Flinn plot (Flinn, 1962; Ramsay, 1967) to discriminate between clusters and
59 girdles of poles. These plots can be useful for three of the five possible fabric symmetry
60 classes – spherical, axial and orthorhombic – because the three fabric eigenvectors coincide
61 with the three symmetry axes. However, there are issues with the interpretation of
62 distributions that are not uniaxial (Woodcock, 1977). We address these issues in this paper.



63 Reches (Reches, 1978; Aydin & Reches, 1982; Reches, 1983; Reches & Dieterich, 1983) has
64 exploited the orthorhombic symmetry of measured quadrimodal fault patterns to explore the
65 relationship between their geometric/ kinematic attributes and tectonic stress. More recently,
66 Yielding (2016) measured the branch lines of intersecting normal faults from seismic
67 reflection data and found they aligned with the bulk extension direction – a feature consistent
68 with their formation as polymodal patterns. Bimodal (i.e. conjugate) fault arrays have branch
69 lines aligned perpendicular to the bulk extension direction.

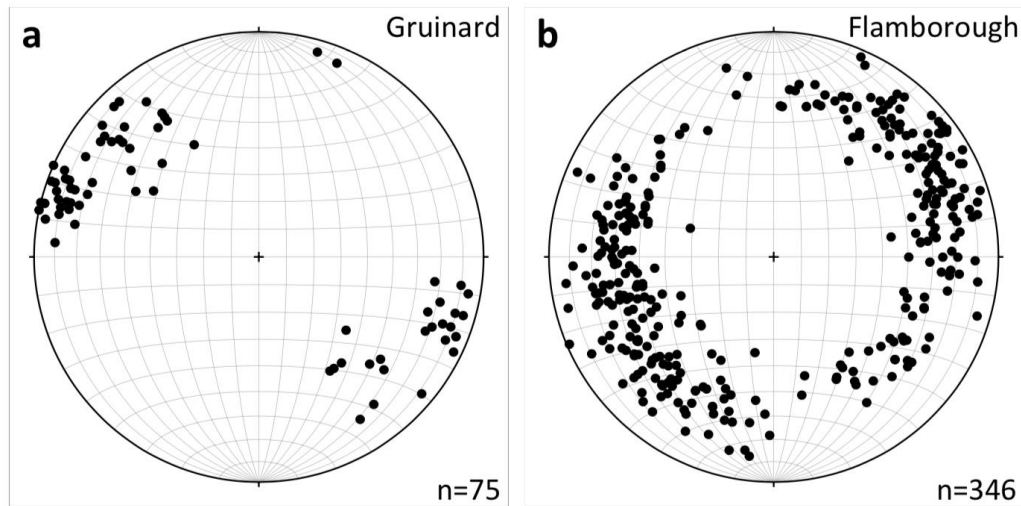
70 1.2 Rationale

71 The fundamental underlying differences in the symmetries of the two kinds of fault pattern –
72 bimodal/bilateral and polymodal/orthorhombic – suggest that we should test for this
73 symmetry using the orientation distributions of measured fault planes. The results of such
74 tests may provide further insight into the kinematics and/or dynamics of the fault-forming
75 process. This paper describes new tests for fault pattern orientation data, and includes the
76 program code for each test written in the R language (R Core Team, 2017). The paper is
77 organised as follows: the next section (2) reviews the kinematic and mechanical issues raised
78 by conjugate and polymodal fault patterns, and in particular, the implications for their
79 orientation distributions. Section 3 describes the datasets used in this study, including
80 synthetic and natural fault orientation distributions. Section 4 presents tests for assessing
81 whether an orientation distribution has orthorhombic symmetry, including a description of
82 the mathematics and the R code. The examples used include synthetic orientation datasets of
83 known attributes (with and without added ‘noise’) and natural datasets of fault patterns
84 measured in a range of rock types. A Discussion of issues raised is provided in Section 5, and
85 is followed by a short Summary. The R code is available from [http://www.mcs.st-](http://www.mcs.st-andrews.ac.uk/~pej/2mode_tests/Rcode190418)
86 [andrews.ac.uk/~pej/2mode_tests/Rcode190418](http://www.mcs.st-andrews.ac.uk/~pej/2mode_tests/Rcode190418).

87

88 2. Bimodal (conjugate) versus quadrimodal fault patterns

89 Conjugate fault patterns should display bimodal or bilateral symmetry in their orientation
90 distributions on a stereogram, and ideally show evidence of central tendency about these two
91 clusters (Figure 1d; Healy et al., 2015). Quadrimodal fault patterns should show orthorhombic
92 symmetry and, ideally, evidence of central tendency about the four clusters of poles on
93 stereograms (Figure 1e). More general polymodal patterns should show orthorhombic
94 symmetry with an even distribution of poles in two arcs (Figure 1f). For data collected from
95 natural fault planes some degree of intrinsic variation, or ‘noise’, is to be expected. Two
96 natural example datasets are shown in Figure 2. The Guinard dataset is from a small area (~
97 5 m²) in one outcrop of Triassic sandstone, and shows poles to deformation bands with small
98 normal offsets (mm-cm). The Flamborough dataset is taken from Peacock & Sanderson (1992;
99 their Figure 2a) and shows poles to normal faults in the Cretaceous chalk along a coastline
100 section of about 1.8 km. The authors clearly state that the approximately E-W orientation of
101 the coastline may have generated a sampling bias in the measured data (i.e. a relative under-
102 representation of E-W oriented fault planes). Both datasets illustrate the nature of the
103 problem addressed in this paper: given variable, incomplete and noisy data of different
104 sample sizes, how can we assess the symmetry of the underlying fault pattern?



105

106 **Figure 2.** Stereographic projections (equal area, lower hemisphere) showing two natural fault
107 datasets. a) Poles to deformation bands (small offset faults; $n=75$) measured in Triassic
108 sandstones at Gruinard Bay, NW Scotland (Healy et al., 2006a, b). These data were collected
109 from a small contiguous outcrop, approximately 10 m² in area. b) Poles to faults measured in
110 Cretaceous chalk at Flamborough Head, NE England ($n=346$). These data have been taken
111 from a figure published in Peacock & Sanderson (1992) and re-plotted in the same format as
112 those from Gruinard.

113

114 3. Datasets used in this study

115 3.1. Synthetic datasets

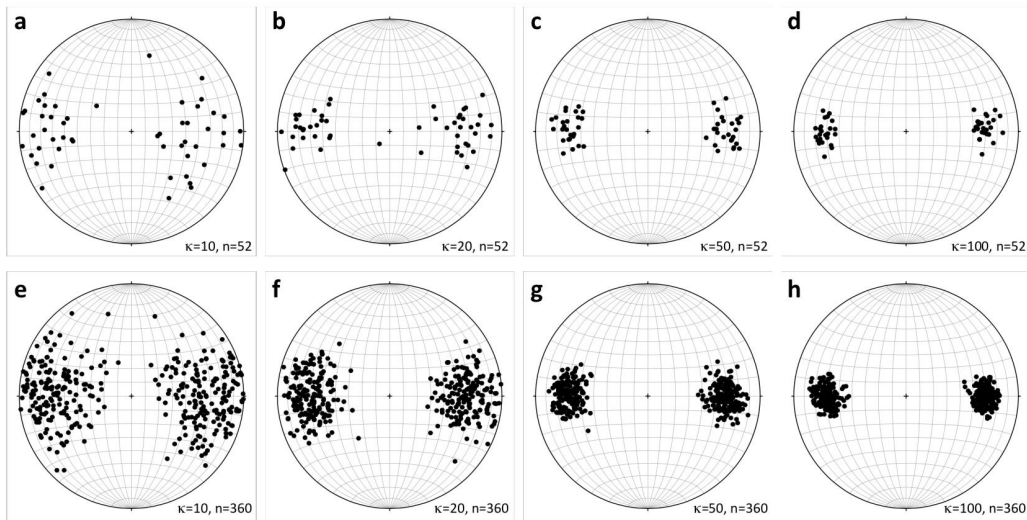
116 We use two sets of synthetic data to test our new statistical methods, both based on the
117 Watson orientation distribution (Fisher et al., 1987 section 4.4.4; Mardia & Jupp, 2000 section
118 9.4.2). This is the simplest non-uniform distribution for describing undirected lines, and has
119 probability density

$$120 \quad f(\pm\mathbf{x}; \boldsymbol{\mu}, \kappa) \propto \exp\{\kappa(\boldsymbol{\mu}^T \mathbf{x})^2\}$$

121 where κ is a measure of concentration (low κ = dispersed, high κ = concentrated) and $\boldsymbol{\mu}$ is the
122 mean direction. To obtain a synthetic conjugate fault pattern dataset of size n we combined
123 two datasets of size $n/2$, each from a Watson distribution, the two mean directions being
124 separated by 60°. We generated synthetic bimodal datasets with $\kappa = 10, 20, 50$ and 100 and
125 $n=52$ and 360 (Figure 3). This variation in κ provides a useful range of concentrations
126 encompassing those observed in measured natural data, and can be considered as a measure
127 of 'noise' within the distribution. Many natural datasets are often small due to limitations of
128 outcrop size, and the two sizes of synthetic distribution ($n=52$ and 360) allow for this fact. For
129 synthetic polymodal fault patterns, we generated quadrimodal datasets of size n by combining
130 four Watson distributions of size $n/4$ with their mean directions separated by 60° in dip (as



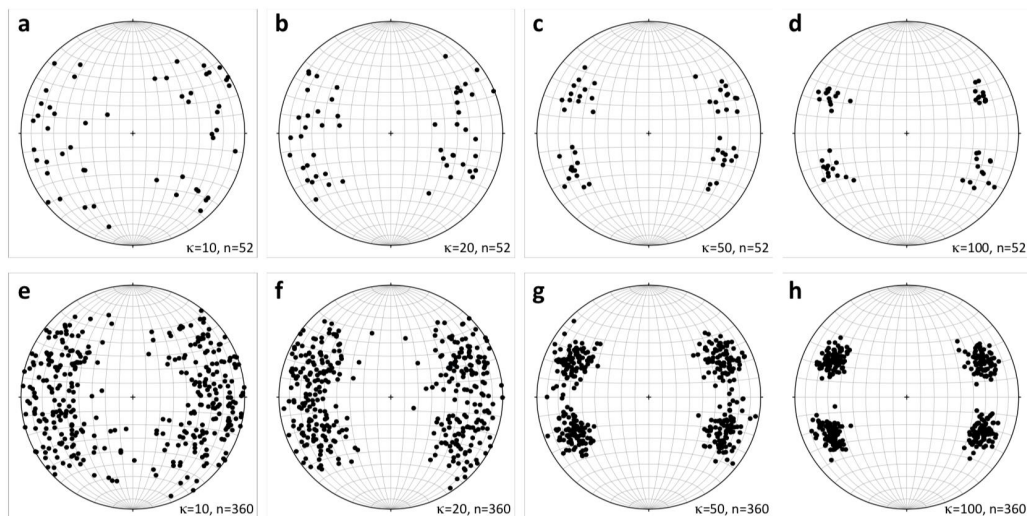
131 above) and 52° in strike (see Healy et al., 2006a, b). By varying n from 52 to 360 we cater for
132 comparisons with smaller and larger natural datasets, and as for the synthetic bimodal
133 datasets, we varied κ in the range 10, 20, 50 and 100 (Figure 4).



134

135 **Figure 3.** Stereographic projections (equal area, lower hemisphere) showing the eight
136 synthetic datasets designed to model conjugate (bimodal) fault patterns in this study. **a-d)**
137 Synthetic fault datasets derived from equal mixtures of two Watson distributions with mean
138 pole directions separated by an inter-fault dip angle of 60 degrees. These models represent a
139 'low fault count' scenario, with $n = 52$ and κ (the Watson dispersion parameter) varying from
140 10 to 100. **e-h)** These models represent a 'high fault count' scenario, with $n = 360$ and
141 κ varying from 10 to 100.

142



143

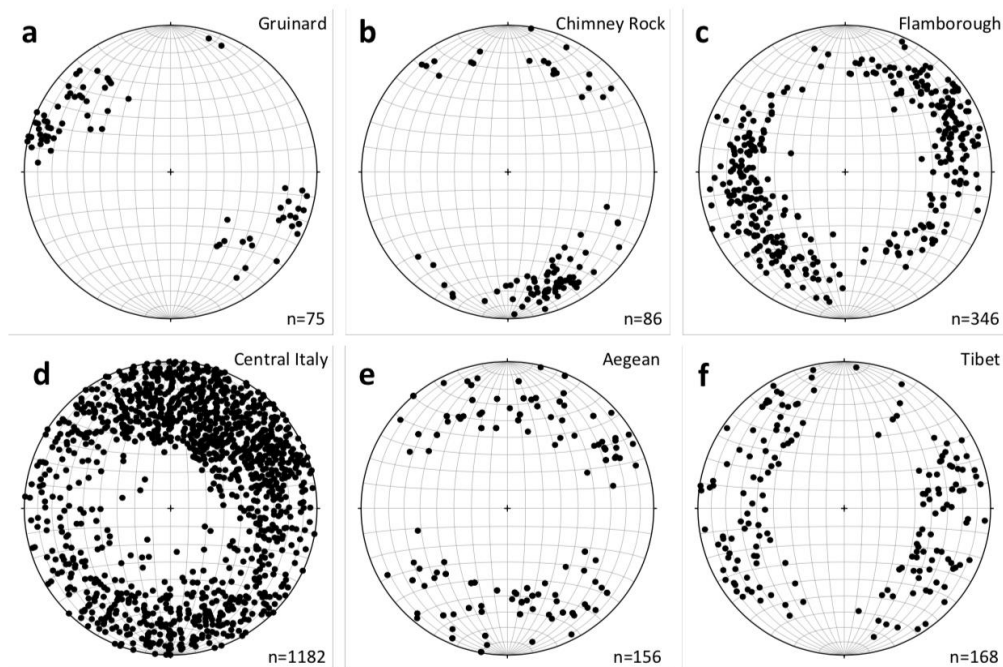


144 **Figure 4.** Stereographic projections (equal area, lower hemisphere) showing the eight
145 synthetic datasets designed to model quadrimodal fault patterns in this study. **a-d)** Synthetic
146 fault datasets derived from equal mixtures of four Watson distributions with mean pole
147 directions separated by an inter-fault dip angle of 60 degrees and a strike separation of 52
148 degrees. These models represent a ‘low fault count’ scenario, with $n = 52$ and κ (the Watson
149 dispersion parameter) varying from 10 to 100. **e-h)** These models represent a ‘high fault
150 count’ scenario, with $n = 360$ and κ varying from 10 to 100.

151

152 3.2. Natural datasets

153 We use six natural datasets of fault plane orientations from regions that have undergone or
154 are currently undergoing extension - i.e. we believe the majority of these faults display normal
155 kinematics (Figure 5). The Gruinard dataset (Figure 5a) is from Gruinard Bay in NW Scotland
156 (UK), and featured in previous publications (Healy et al., 2006a, b). The most important thing
157 about this dataset is that the fault planes were all measured from a small area ($\sim 5 \text{ m}^2$) of
158 contiguous outcrop of a single sandstone bed. This means it is highly unlikely that the
159 orientation data are affected by any local stress variations and subsequent possible rotations.
160 The data were measured in normal-offset deformation bands with displacements of a few
161 millimetres to centimetres. The next three datasets have been digitised from published papers
162 on normal faults in Utah (Figure 5b; Chimney Rock; Krantz, 1989), northern England (Figure
163 5c; Flamborough; Peacock & Sanderson, 1992) and Italy (Figure 5d; Central Italy; Roberts,
164 2007). In each case, the published stereograms were digitised to extract Cartesian (x,y)
165 coordinates of the poles to faults, and these were then converted to plunge and plunge
166 direction using the standard equations for the projection used (e.g. Lisle & Leyshon, 2004).
167 Slight differences in the number of data plotted for each of these three with respect to the
168 original publication arise due to the finite resolution of the digitised image of the stereograms.
169 The last two datasets for the Aegean and Tibet (Figure 5e & f) are derived from earthquake
170 focal mechanisms using the CMT catalogue (Ekström et al., 2012). In each case the steepest
171 dipping nodal plane was selected in the absence of convincing evidence for low-angle normal
172 faulting in these regions.



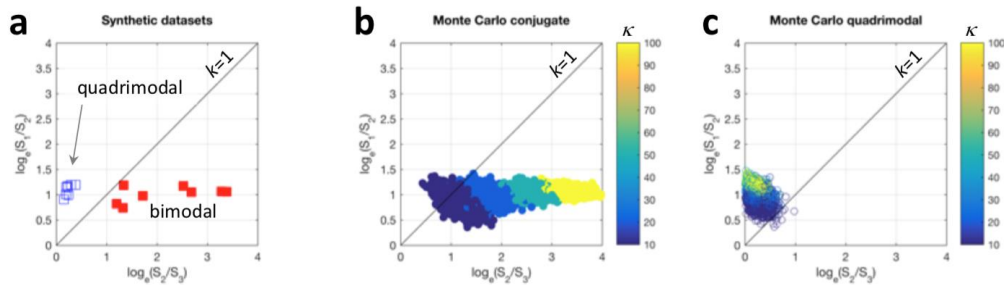
173

174 **Figure 5.** Stereographic projections (equal area, lower hemisphere) showing the six natural
175 datasets used in this study. All plots show poles to faults, the majority of which are inferred to
176 be normal. **a)** Data from deformation bands measured in faulted Triassic sandstones at
177 Gruinard Bay, Scotland (Healy et al., 2006a; 2006b). **b)** Data from faults and measured in
178 sandstones at Chimney Rock in the San Rafael Swell, Utah, USA. Data digitised from Krantz
179 (1989). **c)** Data from faults measured in cliffs of Cretaceous chalk at Flamborough Head, NE
180 England. Data digitised from Peacock & Sanderson (1992). **d)** Data from faults measured in
181 the Apennines of Central Italy. Data digitised from Roberts (2007). **e)** Data from focal
182 mechanism nodal planes derived from the CMT catalogue for the Aegean region (Ekström et
183 al., 2012). **f)** Data from focal mechanism nodal planes derived from the CMT catalogue for the
184 Tibet region (Ekström et al., 2012).

185

186 4. Testing for orthorhombicity

187 4.1 Eigenvalue fabric (modified Flinn) plots



188

189 **Figure 6.** Graphs showing the ratios of eigenvalues of the orientation matrices for the
 190 synthetic datasets (Flinn, 1962; Ramsay, 1967; Woodcock, 1977). **a)** Synthetic conjugate (i.e.
 191 bimodal; filled red symbols) and quadrimodal (hollow blue symbols) fault data. Note that the
 192 conjugate and quadrimodal data lie either side of the line $k = 1$, where $k =$
 193 $\log_e(S_1/S_2)/\log_e(S_2/S_3)$. **b)** Eigenvalue ratios from a Monte Carlo simulation of conjugate fault
 194 orientations using the two Watson mixture model. 1000 simulations were run for each of four
 195 different κ values (10, 20, 50 and 100; a total of 4000 data points), corresponding to the range
 196 of the discrete datasets shown in a). **c)** Eigenvalue ratios from a Monte Carlo simulation of
 197 quadrimodal fault orientations using the four Watson mixture model. 1000 simulations were
 198 run for each of four different κ values (10, 20, 50 and 100; a total of 4000 data points),
 199 corresponding to the range of the discrete datasets shown in a).

200 We calculated the 2nd rank orientation tensor (Woodcock, 1977) for each of the synthetic
 201 datasets shown in Figures 3 and 4 (bimodal and quadrimodal, respectively). The eigenvalues
 202 of this tensor (S_1 , S_2 and S_3 , where S_1 is the largest and S_3 is the smallest) are used to plot the
 203 data on a modified Flinn diagram (Figure 6), with $\log_e(S_2/S_3)$ on the x -axis and $\log_e(S_1/S_2)$ on
 204 the y -axis. The points corresponding to the bimodal (shown in red) and quadrimodal (shown
 205 in blue) datasets lie in distinct areas. Bimodal (conjugate) fault patterns lie below the 1:1 line,
 206 on which $S_1/S_2 = S_2/S_3$. This is due to the S_3 eigenvalue being very low (near 0) for these
 207 distributions, which for high values of κ begin to resemble girdle fabric patterns confined to
 208 the plane of the eigenvectors corresponding to eigenvalues S_1 and S_2 (Woodcock, 1977). In
 209 contrast, the quadrimodal patterns lie above the 1:1 line, as S_3 for these distributions is large
 210 relative to the equivalent bimodal pattern (i.e. for the same values of κ and n). The modified
 211 Flinn plot therefore provides a potentially rapid and simple way to discriminate between
 212 bimodal (conjugate) and quadrimodal fault patterns. Note, however, that the spread of the
 213 bimodal patterns in Figure 6a along the x -axis is a function of the κ value of the underlying
 214 Watson distribution, with low values of κ – low concentration, highly dispersed – lying closer
 215 to the origin. Dispersed or noisy bimodal (conjugate) patterns may therefore lie closer to
 216 quadrimodal patterns (see Discussion below).

217 4.2 Randomisation tests using 2nd and 4th rank orientation tensors

218 4.2.1 Underlying distributions

219 To get a suitable general setting for our tests, we formalise the construction of the bimodal
 220 and quadrimodal datasets considered in Section 3.1. Whereas the datasets considered in



221 Section 3.1 necessarily have equal numbers of points around each mode, for datasets arising
 222 from the distributions here, this is true only *on average*. The very restrictive condition of
 223 having a Watson distribution around each mode is relaxed here to that of having a circularly-
 224 symmetric distribution around each mode.

225 Suppose that axes $\pm\mathbf{x}_1, \dots, \pm\mathbf{x}_n$ are independent observations from some distribution of axes. If
 226 the parent distribution is thought to be multi-modal then two appealing models are:

227 (i) The **bimodal equal mixture model** can be thought of intuitively as obtained by ‘pulling
 228 apart’ a unimodal distribution into two equally strong modes angle α apart. More
 229 precisely, the probability density is:

$$230 \quad f_2(\pm\mathbf{x}; \{\pm\boldsymbol{\mu}_1, \pm\boldsymbol{\mu}_2\}) = \frac{1}{2} \{g(\pm\mathbf{x}; \pm\boldsymbol{\mu}_1) + g(\pm\mathbf{x}; \pm\boldsymbol{\mu}_2)\}, \quad (1)$$

231 where $\pm\boldsymbol{\mu}_1$ and $\pm\boldsymbol{\mu}_2$ are axes angle α apart, and $g(\cdot; \pm\boldsymbol{\mu})$ is the probability density function of
 232 some axial distribution that has rotational symmetry about its mode $\pm\boldsymbol{\mu}$;

233 (ii) The **quadrимodal equal mixture model** can be thought of intuitively as obtained by
 234 ‘pulling apart’ a bimodal equal mixture distribution into two bimodal equal
 235 mixture distributions with planes angle γ apart, so that it has four equally strong modes.
 236 More precisely, the probability density is:

$$237 \quad f_4(\pm\mathbf{x}; \{\pm\boldsymbol{\mu}_1, \pm\boldsymbol{\mu}_2\}, \gamma) = \frac{1}{4} \sum_{\epsilon, \eta} g(\pm\mathbf{x}; \pm\boldsymbol{\mu}_{\epsilon, \eta}), \quad (2)$$

238 where

$$239 \quad \boldsymbol{\mu}_{\epsilon, \eta} = \check{c}\boldsymbol{\nu}_1 + \epsilon s \boldsymbol{\nu}_2 + \eta \check{s} \boldsymbol{\nu}_3 \quad (3)$$

240 with $c = \cos(\alpha/2)$, $s = \sin(\alpha/2)$, $\check{c} = \cos(\gamma/2)$, $\check{s} = \sin(\gamma/2)$, $\cos(\alpha) = \boldsymbol{\mu}'_1 \boldsymbol{\mu}_2$ and (ϵ, η)
 241 runs through $\{\pm 1\}^2$. If $\gamma = 0$, then (3) reduces to (2).

242 The problem of interest is to decide whether the parent distribution is (1) or (2).

243

244 4.2.2 The tests

245 Given axes $\pm\mathbf{x}_1, \dots, \pm\mathbf{x}_n$ we denote by $\pm\hat{\boldsymbol{\nu}}_1$ and $\pm\hat{\boldsymbol{\nu}}_3$, respectively, the largest and smallest
 246 principal axes of the orientation tensor. S_1 and S_3 are the eigenvalues of this matrix. We can
 247 also define

$$248 \quad S_{11} = n^{-1} \sum_{i=1}^n (\hat{\boldsymbol{\nu}}'_1 \mathbf{x}_i)^4, S_{33} = n^{-1} \sum_{i=1}^n (\hat{\boldsymbol{\nu}}'_3 \mathbf{x}_i)^4.$$

249 S_1 and S_2 are the 2nd moments of $\pm\mathbf{x}_1, \dots, \pm\mathbf{x}_n$ along the 1st and 3rd principal axes, respectively,
 250 whereas S_{11} and S_{33} are the 4th moments along these principal axes. Therefore, both $S_1 - S_3$
 251 and $S_{11} - S_{33}$ are measures of anisotropy of $\pm\mathbf{x}_1, \dots, \pm\mathbf{x}_n$.

252 Some algebra shows that

$$253 \quad T_1 - T_3 = \cos(\gamma) \{E[x^2] - E[v^2]\}, \quad (4)$$



254 where T_1 and T_3 are the population versions of S_1 and S_3 , respectively, and $\pm x$ and $\pm v$ are the
 255 components of $\pm \mathbf{x}$ in the quadrimodal equal mixture model (2) along its 1st and 3rd principal
 256 axes, respectively. Then (4) gives

$$257 \quad \cos(\gamma) \approx \frac{S_1 - S_3}{E[x^2] - E[v^2]}$$

258 and therefore, it is sensible to:

259 reject bimodality for *small* values of $S_1 - S_3$. (5)

260 Further algebra shows that

$$261 \quad T_{11} - T_{33} = \cos(\gamma) \{E[x^4] - E[v^4]\}, \quad (6)$$

262 where T_{11} and T_{33} are the population versions of S_{11} and S_{33} , respectively. Then (6) gives

$$263 \quad \cos(\gamma) \approx \frac{S_{11} - S_{33}}{E[x^4] - E[v^4]}$$

264 and so, it is sensible to:

265 reject bimodality for *small* values of $S_{11} - S_{33}$. (7)

266 The significance of tests (5) or (7) is assessed by comparing the observed value of the statistic
 267 with the randomisation distribution. This is achieved by creating a further B pseudo-samples
 268 (for a suitable positive integer B), in each of which the i th observation is obtained from $\pm x_i$ by
 269 rotating $\pm x_i$ about the closer of the 2 fitted modes through a uniformly distributed random
 270 angle. The p -value is taken as the proportion of the $B+1$ values of the statistic that are smaller
 271 than (or equal to) the observed value.

272

273 4.3 Results for synthetic datasets

274 Table 1 gives the p -values and corresponding decisions (at the 5% level) obtained by applying
 275 the tests to some synthetic datasets simulated from the bimodal equal mixture model. Table 2
 276 does the same for some datasets simulated from the quadrimodal equal mixture model. In
 277 each case, both tests come to the correct conclusion.

True number of modes	κ	$S_1 - S_3$ test			$S_{11} - S_{33}$ test		
		n	p -value	# of modes	p -value	# of modes	
2	10	52	0.37	2	0.51	2	
2	10	360	0.27	2	0.33	2	
2	20	52	0.66	2	0.69	2	
2	20	360	0.20	2	0.25	2	
2	50	52	0.45	2	0.48	2	
2	50	360	0.35	2	0.42	2	
2	100	52	0.34	2	0.41	2	



2	100	360	0.60	2	0.63	2
---	-----	-----	------	---	------	---

278

279 **Table 1.** *p*-values and corresponding decisions at 5% significance level of randomisation tests
 280 of bimodality for bimodal equal mixtures of synthetic Watson distributions. *n*=total sample
 281 size. *B*=999 further randomisation samples per data set (see text for details).

282

True number of modes	$S_1 - S_3$ test				$S_{11} - S_{33}$ test	
	κ	<i>n</i>	<i>p</i> -value	# of modes	<i>p</i> -value	# of modes
4	10	52	0.00	> 2	0.00	> 2
4	10	360	0.00	> 2	0.00	> 2
4	20	52	0.00	> 2	0.00	> 2
4	20	360	0.00	> 2	0.00	> 2
4	50	52	0.00	> 2	0.00	> 2
4	50	360	0.00	> 2	0.00	> 2
4	100	52	0.00	> 2	0.00	> 2
4	100	360	0.00	> 2	0.00	> 2

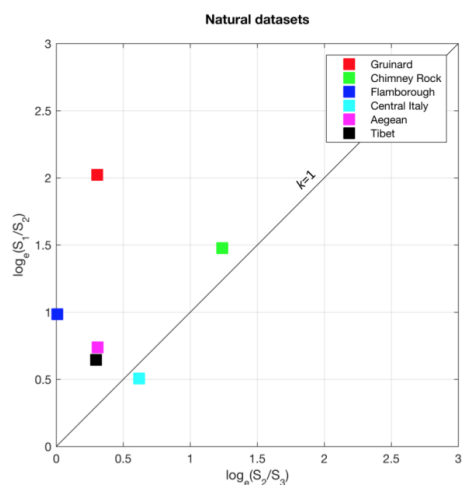
283

284 **Table 2.** *p*-values and corresponding decisions at 5% significance level of randomisation tests
 285 of bimodality for quadrimodal equal mixtures of Watson distributions. *n*=total sample size.
 286 *B*=999 further randomisation samples per data set (see text for details).

287

288 4.4 Results for natural datasets

289 Table 3 gives the *p*-values and corresponding decisions (at the 5% level) obtained by applying
 290 the tests to the natural datasets discussed in Section 3.2. For each dataset, the two tests come
 291 to the same conclusion, which is plausible in view of Figure 5. Figure 7 shows the fabric
 292 eigenvalue plot for these datasets.



293

294 **Figure 7.** Eigenvalue ratio plot for the natural datasets shown in Figure 5. All but one dataset
 295 (Central Italy) lies above the line for $k=1$. The best-constrained quadrimodal fault dataset
 296 (Gruinard) has the highest ratio of $\log_e(S_1/S_2)$.

297

Field location	$S_1 - S_3$ test			$S_{11} - S_{33}$ test	
	n	p -value	# of modes	p -value	# of modes
Gruinard	75	0.00	> 2	0.00	> 2
Chimney Rock	86	0.99	2	1.00	2
Flamborough	346	0.00	> 2	0.00	> 2
Central Italy	1182	0.00	> 2	0.00	> 2
Aegean	156	0.00	> 2	0.00	> 2
Tibet	168	0.00	> 2	0.00	> 2

298

299 **Table 3.** p -values and corresponding decisions at 5% significance level of randomisation tests
 300 of bimodality for natural data sets. n =total sample size. B =999 further randomisation samples
 301 per data set (see text for details).

302

303 5. Discussion

304 In the analysis described above and the tests we performed with synthetic datasets, we
 305 assumed that bimodal and quadrimodal Watson orientation distributions provide a
 306 reasonable approximation to the distributions of poles to natural fault planes. In terms of the
 307 underlying statistics this is unproven, but we know of no compelling evidence in support of
 308 alternative distributions. New data from carefully controlled laboratory experiments on rock

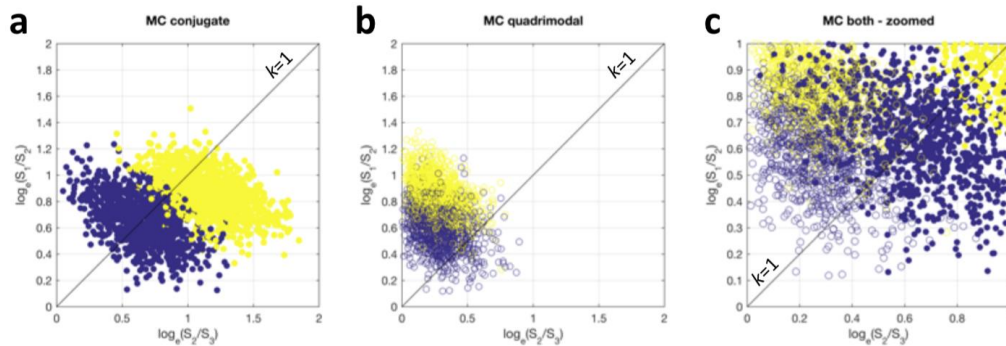


309 or analogous materials might provide important constraints for the underlying statistics of
310 shear fracture plane orientations.

311 We have tested our new methods on synthetic and natural datasets. Arguably, six natural
312 datasets are insufficient to establish firmly the primacy of polymodal orthorhombic fault
313 patterns in nature (Figure 7). However, we reiterate the key recommendation from Healy et
314 al. (2015): to be useful for this task, fault orientation datasets need to show clear evidence of
315 contemporaneity among all fault sets, through tools such as matrices of cross-cutting
316 relationships (Potts & Reddy, 2000). In addition, as shown above, larger datasets ($n > 200$)
317 tend to show clearer patterns. Scope exists to collect fault or shear fracture orientation data
318 from sources other than outcrops: Yielding (2016) has measured normal faults in seismic
319 reflection data from the North Sea and Ghaffari et al. (2014) measured faults in cm-sized
320 samples deformed in the laboratory and then scanned by X-ray computerised tomography.

321 The Chimney Rock dataset is probably not orthorhombic according to the two tests, and lies
322 close to the line for $k=1$ on Figure 7. It is interesting to note that the Chimney Rock data, and
323 other fault patterns from the San Rafael area of Utah, are considered as displaying
324 orthorhombic symmetry by Krantz (1989) and Reches (1978). However, a subsequent re-
325 interpretation by Davatzes et al. (2003) has ascribed the fault pattern to overprinting of
326 earlier deformation bands by later sheared joints. This may account for the inconsistent
327 results of our tests when compared to the position of the pattern on the eigenvalue plot. The
328 Central Italy dataset (taken from Roberts, 2007) is very large ($n=1182$) and the data were
329 measured over a wide geographical area. The dataset lies below the line for $k=1$ on the fabric
330 eigenvalue plot (Figure 7), which might suggest it is bimodal. However, for fault planes
331 measured over large areas there is a significant chance that regional stress variations may
332 have produced systematically varying orientations of fault planes.

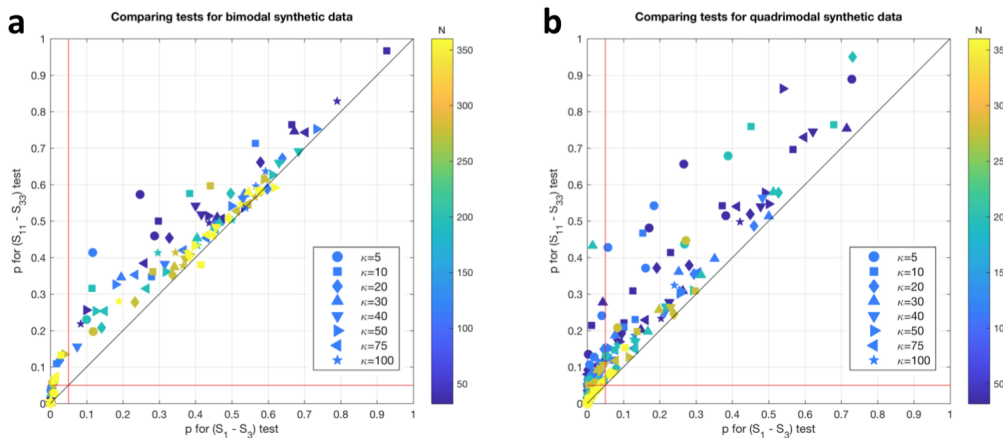
333 A final point concerns dispersion (noise) in the data. Synthetic datasets of bimodal
334 (conjugate) and quadrimodal patterns with low values of κ ; the Watson concentration
335 parameter, fall into overlapping fields on the eigenvalue fabric plot. We ran 1000 Monte Carlo
336 simulations of bimodal and quadrimodal Watson distributions each with $n=52$ poles, and $\kappa =$
337 5 and 10, and the results are shown in Figure 8. Bimodal (conjugate) datasets for these
338 dispersed and sparse patterns lie across the 1:1 line on the fabric plot (Figure 8a; $\kappa = 5$ in
339 blue, $\kappa = 10$ in yellow). Quadrimodal datasets for these parameters are also noisy, with some
340 fabrics lying below the 1:1 line (Figure 8b; $\kappa = 5$ in blue, $\kappa = 10$ in yellow). Under these
341 conditions of low κ (dispersed) and low n (sparse), it can be difficult to separate bimodal
342 (conjugate) from quadrimodal fault patterns. However, we assert that this may not matter: a
343 noisy and disperse 'bimodal' conjugate fault pattern is in effect similar to a polymodal pattern
344 i.e. slip on these dispersed fault planes will produce a bulk 3D triaxial strain.



345

346 **Figure 8.** Eigenvalue ratio plots of synthetic data to illustrate the impact of dispersion on the
 347 ability of this plot to discriminate between conjugate (bimodal) and quadrimodal fault data.
 348 **a)** Monte Carlo ensemble of 2000 conjugate fault populations (mixtures of two equal Watson
 349 distributions), with κ varying from 5 (dark blue) to 10 (yellow). **b)** Monte Carlo ensemble of
 350 2000 quadrimodal fault populations (mixtures of four equal Watson distributions), with κ
 351 varying from 5 (dark blue) to 10 (yellow). **c)** Data from a) and b) merged onto the same plot
 352 and enlarged to show the region close to the origin. Note the considerable overlap between
 353 the conjugate (bimodal) data with the quadrimodal data, especially for $\kappa = 5$ (dark blue).

354 To assess the relative performance of the two tests presented in this paper, we generated
 355 synthetic bimodal and quadrimodal distributions and compared the resulting p-values from
 356 applying both the S_1 - S_3 and S_{11} - S_{33} tests to the same data. The results are shown in Figure 9,
 357 displayed as cross-plots of $p(S_1$ - $S_3)$ versus $p(S_{11}$ - $S_{33})$. While there is a slight tendency for the
 358 p-values from the S_{11} - S_{33} test to exceed those of the S_1 - S_3 test (i.e. the points tend on average
 359 to plot above the 1:1 line), neither of the tests can be said to 'better' or more 'accurate'. We
 360 therefore recommend the S_1 - S_3 test as simpler and sufficient.



361

362 **Figure 9.** Eigenvalue ratio plots comparing the relative performance of the two tests
 363 proposed in this paper. The red lines denote p-values for either test at $p=0.05$, and the
 364 diagonal black line is the locus of points where $p(S_1$ - $S_3) = p(S_{11}$ - $S_{33})$. **a)** For bimodal synthetic



365 datasets with size (N) varying from 32-360 and concentration (κ) varying from 5-100, both
366 tests perform well and reject the majority of the datasets ($p \gg 0.05$). The p-values for the S_{11} -
367 S_{33} test are, on average, slightly higher than those for the S_1 - S_3 test across a range of dataset
368 sizes and concentrations. **b)** For quadrimodal synthetic datasets, many of the p-values are <
369 0.05, and this especially true for the larger datasets (higher N, green/yellow). Smaller datasets
370 (blue) can return p-values > 0.05.

371

372 **6. Summary**

373 Bimodal (conjugate) fault patterns form in response to a bulk plane strain with no extension
374 in the direction parallel to the mutual intersection of the two fault sets. Quadrimodal and
375 polymodal faults form in response to bulk triaxial strains and probably constitute the more
376 general case for brittle deformation on a curved Earth (Healy et al., 2015). In this
377 contribution, we show that distinguishing bimodal from quadrimodal fault patterns based on
378 the orientation distribution of their poles can be achieved through the eigenvalues of the 2nd
379 and 4th rank orientation tensors. We present new methods and new open source software
380 written in R to test for these patterns. Tests on synthetic datasets where we controlled the
381 underlying distribution to be either bimodal (i.e. conjugate) or quadrimodal (i.e. polymodal,
382 orthorhombic) demonstrate that a combination of fabric eigenvalue (modified Flinn) plots
383 and our new randomisation tests can succeed. Applying the methods to natural datasets from
384 a variety of extensional normal-fault settings shows that 5 out of the 6 fault patterns
385 considered here are probably polymodal. The most tightly constrained natural dataset
386 (Gruinard) displays clear orthorhombic symmetry and is unequivocally polymodal. We
387 encourage other workers to apply these tests to their own data and assess the underlying
388 symmetry in the brittle fault pattern and to consider what this means for the causative
389 deformation.

390

391 **Acknowledgements**

392 DH gratefully acknowledges receipt of NERC grant NE/N003063/1, and thanks the School of
393 Geosciences at the University of Aberdeen for accommodating a period of study leave, during
394 which time this paper was written.

395

396 **References**

- 397 Aydin, A., & Reches, Z. E. 1982. Number and orientation of fault sets in the field and in
398 experiments. *Geology*, 10(2), 107-112.
- 399 Blenkinsop, T. G. 2008. Relationships between faults, extension fractures and veins, and
400 stress. *Journal of Structural Geology*, 30(5), 622-632.



- 401 Davatzes, N.C., Aydin, A. and Eichhubl, P., 2003. Overprinting faulting mechanisms during the
402 development of multiple fault sets in sandstone, Chimney Rock fault array, Utah, USA.
403 *Tectonophysics*, 363(1-2), pp.1-18.
- 404 Ekström, G., Nettles, M., & Dziewoński, A. M. 2012. The global CMT project 2004–2010:
405 Centroid-moment tensors for 13,017 earthquakes. *Physics of the Earth and Planetary Interiors*,
406 200, 1-9.
- 407 Fisher, N.I., Lewis, T. and Embleton, B.J., 1987. *Statistical analysis of spherical data*. Cambridge
408 University Press.
- 409 Flinn, D. 1962. On folding during three-dimensional progressive deformation. *Quarterly*
410 *Journal of the Geological Society*, 118(1-4), 385-428.
- 411 Ghaffari, H. O., Nasser, M. H. B., & Young, R. P. 2014. Faulting of Rocks in a Three-Dimensional
412 Stress Field by Micro-Anticracks. *Scientific reports*, 4, 5011.
- 413 Healy, D., Jones, R.R. and Holdsworth, R.E., 2006a. Three-dimensional brittle shear fracturing
414 by tensile crack interaction. *Nature*, 439(7072), pp.64-67.
- 415 Healy, D., Jones, R.R. and Holdsworth, R.E., 2006b. New insights into the development of
416 brittle shear fractures from a 3-D numerical model of microcrack interaction. *Earth and*
417 *Planetary Science Letters*, 249(1), pp.14-28.
- 418 Healy, D., Blenkinsop, T.G., Timms, N.E., Meredith, P.G., Mitchell, T.M. and Cooke, M.L., 2015.
419 Polymodal faulting: Time for a new angle on shear failure. *Journal of Structural Geology*, 80,
420 pp.57-71.
- 421 Krantz, R. W. 1989. Orthorhombic fault patterns: the odd axis model and slip vector
422 orientations. *Tectonics*, 8(3), 483-495.
- 423 Lisle, R. J., & Leyshon, P. R. 2004. *Stereographic projection techniques for geologists and civil*
424 *engineers*. Cambridge University Press.
- 425 Mardia, K.V. & Jupp, P.E., 2000. *Directional statistics*. John Wiley & Sons.
- 426 McCormack, K.D. & McClay, K.R., 2018. Orthorhombic faulting in the Beagle Sub-basin, North
427 West Shelf, Australia. *Geological Society, London, Special Publications*, 476.
- 428 Peacock, D. C. P., & Sanderson, D. J. 1992. Effects of layering and anisotropy on fault geometry.
429 *Journal of the Geological Society*, 149(5), 793-802.
- 430 Potts, G. J., & Reddy, S. M. 2000. Application of younging tables to the construction of relative
431 deformation histories—1: fracture systems. *Journal of Structural Geology*, 22(10), 1473-1490.
- 432 R Core Team, 2017. *R: A language and environment for statistical computing*. R Foundation for
433 Statistical Computing, Vienna, Austria. URL <https://www.R-project.org/>.
- 434 Ramsay, J. 1967. Folding and fracturing of rocks.



- 435 Reches, Z. E. 1978. Analysis of faulting in three-dimensional strain field. *Tectonophysics*, 47(1-
436 2), 109-129.
- 437 Reches, Z. E. 1983. Faulting of rocks in three-dimensional strain fields II. Theoretical analysis.
438 *Tectonophysics*, 95(1-2), 133-156.
- 439 Reches, Z. E., & Dieterich, J. H. 1983. Faulting of rocks in three-dimensional strain fields I.
440 Failure of rocks in polyaxial, servo-control experiments. *Tectonophysics*, 95(1-2), 111-132.
- 441 Roberts, G. P. 2007. Fault orientation variations along the strike of active normal fault systems
442 in Italy and Greece: Implications for predicting the orientations of subseismic-resolution
443 faults in hydrocarbon reservoirs. *AAPG bulletin*, 91(1), 1-20.
- 444 Scheidegger, A. E. 1965. On the statistics of the orientation of bedding planes, grain axes, and
445 similar sedimentological data. *US Geological Survey Professional Paper*, 525, 164-167.
- 446 Woodcock, N.H., 1977. Specification of fabric shapes using an eigenvalue method. *Geological*
447 *Society of America Bulletin*, 88(9), pp.1231-1236.
- 448 Yielding, G., 2016. The geometry of branch lines. In: Childs, C., Holdsworth, R. E., Jackson, C.
449 A.-L., Manzocchi, T., Walsh, J. J. & Yielding, G. (eds). *The Geometry and Growth of Normal Faults*.
450 Geological Society, London, Special Publications, 439.
- 451